



Janus photoelectrocatalytic filter for sustainable water decontamination



Limin Jin ^a, Meng Sun ^b, Jianping Yang ^c, Yingping Huang ^d, Yanbiao Liu ^{a,e,*}

^a College of Environmental Science and Engineering, Textile Pollution Controlling Engineering Center of Ministry of Environmental Protection, Donghua University, Shanghai 201620, China

^b Center for Water and Ecology, State Key Joint Laboratory of Environment Simulation and Pollution Control, School of Environment, Tsinghua University, Beijing 100084, China

^c State Key Laboratory for Modification of Chemical Fibers and Polymer Materials, College of Materials Science and Engineering, Donghua University, Shanghai 201620, China

^d College of Hydraulic & Environmental Engineering, China Three Gorges University, Yichang 443002, China

^e Shanghai Institute of Pollution Control and Ecological Security, 1239 Siping Road, Shanghai 200092, China

ARTICLE INFO

Keywords:

Janus filter
Hydrogen peroxide
Hydroxy radical
Photoelectrocatalytic process
Water decontamination

ABSTRACT

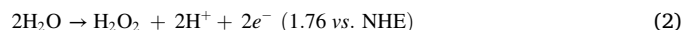
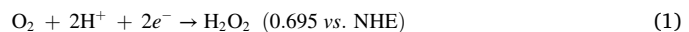
Herein, we conceive a Janus photoelectrocatalytic filter (Sb-Fe/MXene) by depositing Sb single-atoms (Sb-SA) and Fe nanoclusters (Fe-NC) decorated MXene mixture on either side of Ni-foam substrate, respectively, which realized sustainable and efficient generation of hydrogen peroxide (H_2O_2) and hydroxy radical ($^{\bullet}OH$) without any chemicals input. Photocatalytic-side ensures that the accumulated holes at Ti vacancies neighboring the Sb-SA promote the $4e^-$ water oxidation reactions to produce O_2 , while the Sb-SA sites collect electrons forming reducing centers for non-sacrificial H_2O_2 production via the $2e^-$ oxygen reduction reaction. Electrocatalytic-side guarantees the circulation of $\equiv Fe(III)/\equiv Fe(II)$ by continuously exposing “fresh” reactive sites by dissociating H_2O_2 on the $\equiv Fe(II)$. This further prohibits iron sludge accumulation with an enhanced remedy of micro-pollutants, even under neutral conditions for wastewater. The collaborative effect between photochemistry and electrochemistry establishes a strategy for energy conversion and environmental remediation using a Janus photoelectrocatalytic filtration system.

1. Introduction

Advanced oxidation processes (AOPs) are state-of-the-art approaches applied for the decontamination of organic pollutants in water by producing oxidative radicals (e.g., $^{\bullet}OH$) from soluble oxidants (e.g., H_2O_2) [1,2]. Those $^{\bullet}OH$ can unselectively oxidize the organic molecules and eventually mineralize them into harmless inorganic molecules (e.g., CO_2 , H_2O , and inorganic ions) [3]. Strong oxidants such as H_2O_2 have the potential capacity to generate $^{\bullet}OH$. However, this inevitably increased the operational cost and led to elevated safety risks associated with the storage and transportation of chemicals [4]. So far, the effective activation of H_2O_2 also remains unsatisfactory.

In situ producing H_2O_2 from $2e^-$ oxygen reduction or water oxidation processes, described in Eq. 1-2, have been proposed to reduce the overall cost, which can be realized via photocatalysis or electrocatalysis [5,6]. Extensive efforts have been devoted to the electrocatalytic H_2O_2 generation, yet, few device-level demonstrations have been practically

implemented mainly due to its high energy cost [7]. Alternatively, photocatalytic H_2O_2 synthesis on semiconductors has emerged as an energy-saving approach. To improve the H_2O_2 yield through photocatalysis, the oxygen reduction reaction (ORR, Eq. 1) and water oxidation reaction (WOR, Eq. 3) must be improved collectively, since O_2 produced in WOR is needed in the ORR [8,9]. Boosted reaction kinetics can be envisaged once the *in situ* generated O_2 from the $4e^-$ WOR were utilized efficiently by the $2e^-$ ORR. Therefore, it is highly desirable to balance the kinetics of WOR and ORR in a delicately-designed photocatalytic system to maximize the H_2O_2 production and overcome the limitation of direct producing H_2O_2 from $2e^-$ WOR at a high potential of + 1.76 V vs. normal hydrogen electrode (NHE) [10].



* Corresponding author at: College of Environmental Science and Engineering, Textile Pollution Controlling Engineering Center of Ministry of Environmental Protection, Donghua University, Shanghai 201620, China.

E-mail address: yanbiaoliu@dhu.edu.cn (Y. Liu).



Introducing metal cations as the catalytic sites can improve the ORR efficiency and selectivity. It has been reported that the Pauling-type (end-on) adsorption of O_2 molecules onto metal sites is highly desirable for selective $2e^-$ ORR, while other Griffiths and Yeager types (side-on) tend to split the O–O bonds, resulting in a high selectivity for $4e^-$ ORR (Eq. 4) [11,12]. On the atomically isolated sites in single-atom catalysts (SACs), O_2 molecules are usually chemisorbed with an end-on configuration, thus rendering the $2e^-$ ORR pathway dominant [13]. However, most transition metal elements with partially filled d bands, including Fe, Mn, Ni, Co, and Cu, can cause high-rate recombination of photogenerated charge carriers [14]. Teng et al., [15] reported that constructing SACs with a fully occupied d orbital can achieve efficient charge separation by preventing the creation of an intermediate band. This would be conducive to the photocatalytic synthesis of H_2O_2 through the pathway of the $2e^-$ ORR. Thus, developing an antimony single-atom (Sb-SA) photocatalyst with the d^{10} electronic configuration would be an ideal candidate for photocatalytic H_2O_2 synthesis via the $2e^-$ ORR.

Regarding the transformation of H_2O_2 , the traditional Fenton process mainly relies on the $\equiv \text{Fe(III)}/\equiv \text{Fe(II)}$ circulation to generate $\bullet\text{OH}$, but suffers from the sluggish reaction kinetics (Eqs. 5–6; $0.001\text{--}0.01 \text{ m}^{-1}\cdot\text{s}^{-1}$) owing to iron sludge accumulation [16–18]. This could be partially addressed by driving the circulation of $\equiv \text{Fe(III)}/\equiv \text{Fe(II)}$ (Eq. 7) using an external electric field [19,20]. Compared with aggregated metal nanoparticles, Fe nanoclusters (Fe-NC) can expose much more active sites and thus achieve higher atom utilities assisted with the electric field [21]. To this end, MXene has been recognized as an ideal matrix to support catalytic sites thanks to its unique photoelectrochemical property [22]. For example, single-layered $\text{Ti}_3\text{C}_2\text{T}_x$ MXene can be fabricated from bulk Ti_3AlC_2 using HF etching to dissolve Al layers, leaving abundant terminal groups “ T_x ” ($-\text{O}$, $-\text{OH}$, and $-\text{F}$) on the MXene surface to anchor metal precursors via electrostatic attraction [23]. The single-layered MXene can also be facilely assembled into three-dimensional channel conductive networks, enabling flow-through operation [24,25]. Notably, most reported photoelectrocatalytic systems focus only on half-cell reactions (either anodic oxidation or cathodic reduction) [26]. Thus, the redox processes are only partially utilized. Hence, rationally designing a flow-through photoelectrocatalytic system to utilize both reduction and oxidation reactions could be a novel strategy for efficient environmental applications [27], featuring enhanced reaction kinetics and Faradaic efficiency at low energy consumption.

Here, a Janus photoelectrocatalytic filter (Sb-Fe/MXene) that features double-sided reactive surfaces is designed on a Ni-foam substrate. One side is constructed by depositing MXene solution decorated with Sb-SA to facilitate the photochemical reaction, while the other side is formed by depositing MXene solution modified by Fe-NC to boost the electrochemical reaction. In the photocatalytic-active side, O_2 adsorbed on the Sb-SA sites with an end-on configuration, which is photocatalytically converted to the Sb-peroxide species (Sb-OOH) through a selective $2e^-$ ORR process to form H_2O_2 . Simultaneously, those accumulated holes at Ti vacancies neighboring the Sb-SA sites facilitated the $4e^-$ WOR. On the electrocatalytic-active side, rapid circulation between $\equiv \text{Fe(III)}$ and $\equiv \text{Fe(II)}$ promotes the transformation of H_2O_2 to $\bullet\text{OH}$ by controlling the oxidation states of Fe-NC with the applied electric field. We then evaluated the performance of the Janus photoelectrocatalytic filtration system for decontamination water containing sulfamethoxazole (SMX) as the representative organic contaminant. An enhanced

SMX degradation kinetics can be expected thanks to the synergistic effects of convection-enhanced mass transport, abundant reactive sites, and the Janus design. This work provides a promising Janus photoelectrocatalytic filter to address the production and activation of H_2O_2 in a single operational unit, which provides a novel design of a highly efficient water decontamination system.

2. Materials and methods

2.1. Synthesis of Sb-Fe/MXene filter

$\text{Ti}_3\text{C}_2\text{T}_x$ MXene was prepared by chemical etching of bulky Ti_3AlC_2 with diluted HF (40 wt%, Text S1 and S2) [28]. In a typical synthesis of the Sb-SA/MXene, 25.0 mg of $\text{Ti}_3\text{C}_2\text{T}_x$ was firstly dissolved in 25.0 mL of ethanol in a round-bottom flask, followed by ultra-sonication for 40 min to obtain a uniform dispersion under Ar atmosphere. Then, 2.0 mL of $\text{C}_8\text{H}_4\text{K}_2\text{O}_{12}\text{Sb}_2\cdot 3 \text{ H}_2\text{O}$ (1.0 mg/mL) was added to the $\text{Ti}_3\text{C}_2\text{T}_x$ suspension slowly to obtain Sb-SA/MXene solution under ultra-sonication. Fe-NC/MXene can be prepared similarly to the Sb-SA/MXene, except for the added amount of $\text{FeCl}_3\cdot 3 \text{ H}_2\text{O}$ (3.0 mL of 5.0 mg/mL) and $\text{N}_2\text{H}_4\cdot \text{H}_2\text{O}$ (1.0 mL).

The Janus Sb-Fe/MXene filter can be prepared via pressure-assisted spray [27]. The Sb-SA/MXene and Fe-NC/MXene solution was sputter-coated onto the feed- and permeate-side of a modified Ni-foam substrate (7.1 cm^2), respectively, using a sputtering gun equipped with a 0.3 mm nozzle at a working pressure of 0.2 MPa provided by Ar. The sputtering target materials were positioned in a tetrahedral layout 15.0 cm away from the Ni-foam substrate at a 90.0° . The deposition quantity for the Sb-SA/MXene and Fe-NC/MXene functionalized surfaces was $\sim 2.6 \text{ mg/cm}^2$ each. Details on the characterization details for the Janus Sb-Fe/MXene filter were available in Text S3.

2.2. Photoelectrochemical activity evaluation

The photoelectrochemical measurements were carried out in a commercial Whatman polycarbonate casing with photoelectrochemistry modifications (Fig. S1) [24,29]. The obtained Janus Sb-Fe/MXene filter was loaded between the feed and permeate chamber, while Sb-SA/MXene side faced the feeding chamber and Fe-NC/MXene side faced the permeate chamber. The photo-responsive Sb-SA/MXene side utilized O_2 to produce H_2O_2 via photocatalytic route, while the Fe-NC/MXene side served as cathode to decompose the as-generated H_2O_2 to generate $\bullet\text{OH}$. All experiments were performed in a phosphate buffer solution at a pH of 6.8 and a flow rate of 6.0 mL/min. The efficacy of the Sb-Fe/MXene filter was also challenged with real lake water (50.0 mL) spiked with 2.0 mg/L Sb(III) and 10.0 mg/L SMX. Exhausted filter were washed with deionized water and dried under a vacuum overnight to initiate another cycle under similar procedures.

2.3. Analytical procedures

The concentration of H_2O_2 was determined using the potassium permanganate titration method as well as the potassium titanium oxalate spectrophotometric method [30]. The concentration of SMX was analyzed by high-performance liquid chromatography (HPLC; Thermo Fisher Scientific) equipped with a column Eclipse plus-C18 (4.6 \times 100 mm, 3.5 μm) using a 0.1 vol% phosphoric acid/methanol (40/60, v/v) mobile phase (isocratic elution) at a flow rate of 1.0 mL/min; the detection wavelength was 286 nm. Reactive oxygen species (ROS) were detected by electron paramagnetic resonance (EPR) spectroscopy (EMXnano, Bruker, Germany) with 5,5-dimethyl-1-pyrroline-n-oxide (DMPO) or 2,6,6-tetramethyl-4-piperidinyl (TEMP) as spin trapping agents.

3. Results and discussion

3.1. Characterization of Sb-SA/MXene surface

The preparation process of Janus Sb-Fe/MXene filter via a “self-reduction” strategy was systematically expounded in Fig. 1a. This can be achieved by creating the $\text{Ti}_3\text{C}_2\text{T}_x$ MXene layer with a high density of Ti vacancy as the substrate with a reduction property. During the fabrication of single-layered $\text{Ti}_3\text{C}_2\text{T}_x$ MXene (Figs. S2 and S3), certain neighboring Ti atoms were removed to form Ti vacancies surrounded by abundant terminal groups, including $-\text{F}$, $-\text{OH}$, and $-\text{O}$. High-angle annular dark-field scanning transmission electron microscopy (HAADF-STEM) image (Fig. S4) confirmed the presence of Ti vacancies, further verified via elemental analysis (Table S1). The weight ratio of Ti atoms to C atoms in the $\text{Ti}_3\text{C}_2\text{T}_x$ is 0.65, lower than that in the Ti_3AlC_2 (0.72). Those Ti vacancies were unstable and reactive, consequently, the added Sb^{3+} ions were attracted electrostatically by surface terminal groups around the Ti vacancy sites. With the formation of Sb–O bonds, the strong Sb–O covalent bonds interaction is essential for forming atomically dispersed stable Sb-SA.

The crystalline phase and surface morphologies of the Sb-SA/MXene exhibited no evident changes compared with the undoped $\text{Ti}_3\text{C}_2\text{T}_x$ MXene, confirmed by XRD and the high-resolution transmission electron microscopy (HRTEM) results (Figs. S5 and S6). The cross-section view clearly demonstrated a typical laminar structure and uniform 2D nanochannels with a thickness of $3.2 \pm 0.5 \mu\text{m}$ (Fig. 1b). The HAADF-STEM image shows that high-density bright dots assigned to the individual Sb atoms (cycled in Fig. 1c) are evenly distributed on the MXene surface. The size profile in the inset in Fig. 1c revealed the average size of the bright spots is less than 0.2 nm, confirming the formation of Sb-SA. In addition, the element mapping in Fig. S6 showed that the elements of Ti, C, O, and Sb were evenly distributed with the Sb contents of 2.8 wt%, which is significantly higher than single-atom species in the reported SACs with transition metals [31,32].

X-ray photoelectron spectroscopy (XPS) and X-ray absorption

spectroscopy (XAS) was used to elucidate the electronic property and coordination environment of the as-prepared Sb-SA/MXene [33,34]. XPS spectra (Fig. 1e) confirmed the presence of Sb in the Sb-SA/MXene with the peaks at 539.4 and 529.4 eV, assigned to the Sb^{3+} $3\text{d}_{3/2}$ and $3\text{d}_{5/2}$. These binding energies are slightly less than that in the Sb_2O_3 (539.6 and 530.6 eV) [35], suggesting the substitutional Sb^{3+} in the Sb-SA/MXene led to an increase in electron cloud density. The X-ray absorption fine structure spectroscopy (XANES) results (Fig. 1f) show that for the Sb-SA/MXene, the Sb K-edge is higher than the Sb foil by 2.7 eV and less than the Sb_2O_3 by 0.2 eV, confirming the Sb is charged slightly less than +3, agreed with the XPS results. An extended X-ray absorption fine structure (FT-EXAFS) spectrum (Fig. 1g) was collected in the k -space (k^3 -weighted), shown in Fig. S7. Sb-SA/MXene exhibited a single feature at 1.55 \AA , corresponding to the Sb–O bonds. More importantly, no feature associated with Sb–Sb bond (2.65 \AA) was observed, confirming the atomically dispersed Sb. The wavelet transform (WT) contour plots (Fig. S8) of Sb-SA/MXene displayed only one contour at 5.0 \AA^{-1} , mainly corresponding to the Sb–O scattering, consistent with the formation of Sb-SA. The Sb coordination was further evaluated by analyzing the EXAFS data (Fig. 1h and Table S2), which suggested the Sb atom is coordinated with 3.2 O atoms on the MXene nanosheets. Moreover, two Sb–C bonds were formed according to the fitted curve due to the overlapping orbitals of Sb and surrounding C atoms, agreeing with the DFT calculations (Fig. S9). All the above results unambiguously confirmed that single Sb atoms had been successfully immobilized on the MXene nanosheets using the *in situ* “self-reduction” approach.

3.2. Photocatalytic H_2O_2 production on Sb-SA/MXene surface

These Sb-SA/MXene nanosheets were sputtered onto the feed-side of a Ni-foam to boost H_2O_2 production under visible light from water with dissolved oxygen without any sacrificial agent (Fig. 2a). Sb-SA/MXene showed the highest H_2O_2 production rate ($343.4 \mu\text{mol/L}$ within 90 min in phosphate buffer solution, Fig. 2b) among all the tested

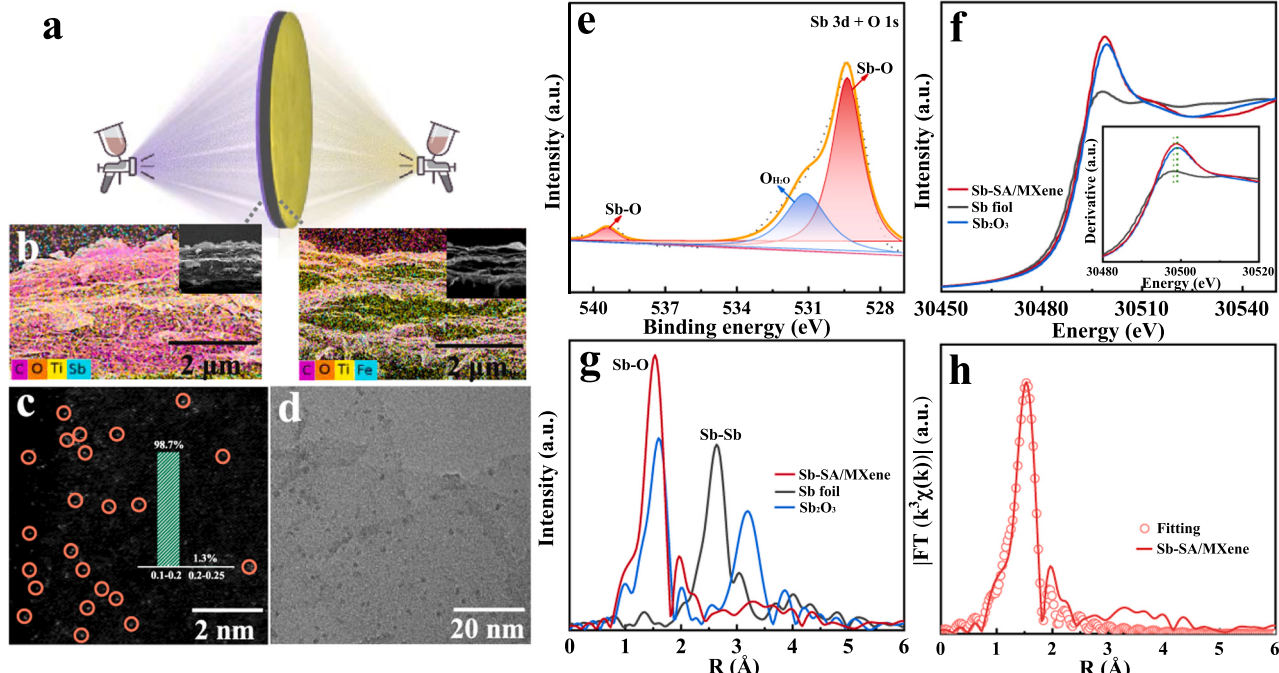


Fig. 1. Fabrication and characterization of the Sb-Fe/MXene filter. (a) Schematic depicting the fabrication of the Sb-Fe/MXene by the sputtered method. (b) SEM cross-section images of the Sb-SA/MXene and Fe-NC/MXene surfaces. (c) High-magnification HAADF-STEM image of Sb-SA/MXene surface. (d) HRTEM image of Fe-NC/MXene surface. (e) XPS spectra of the Sb 3d on the Sb-SA/MXene surface. (f) XANES spectra of Sb foil, Sb_2O_3 and Sb-SA/MXene. (h) Fitting of the EXAFS data of Sb-SA/MXene in R space.

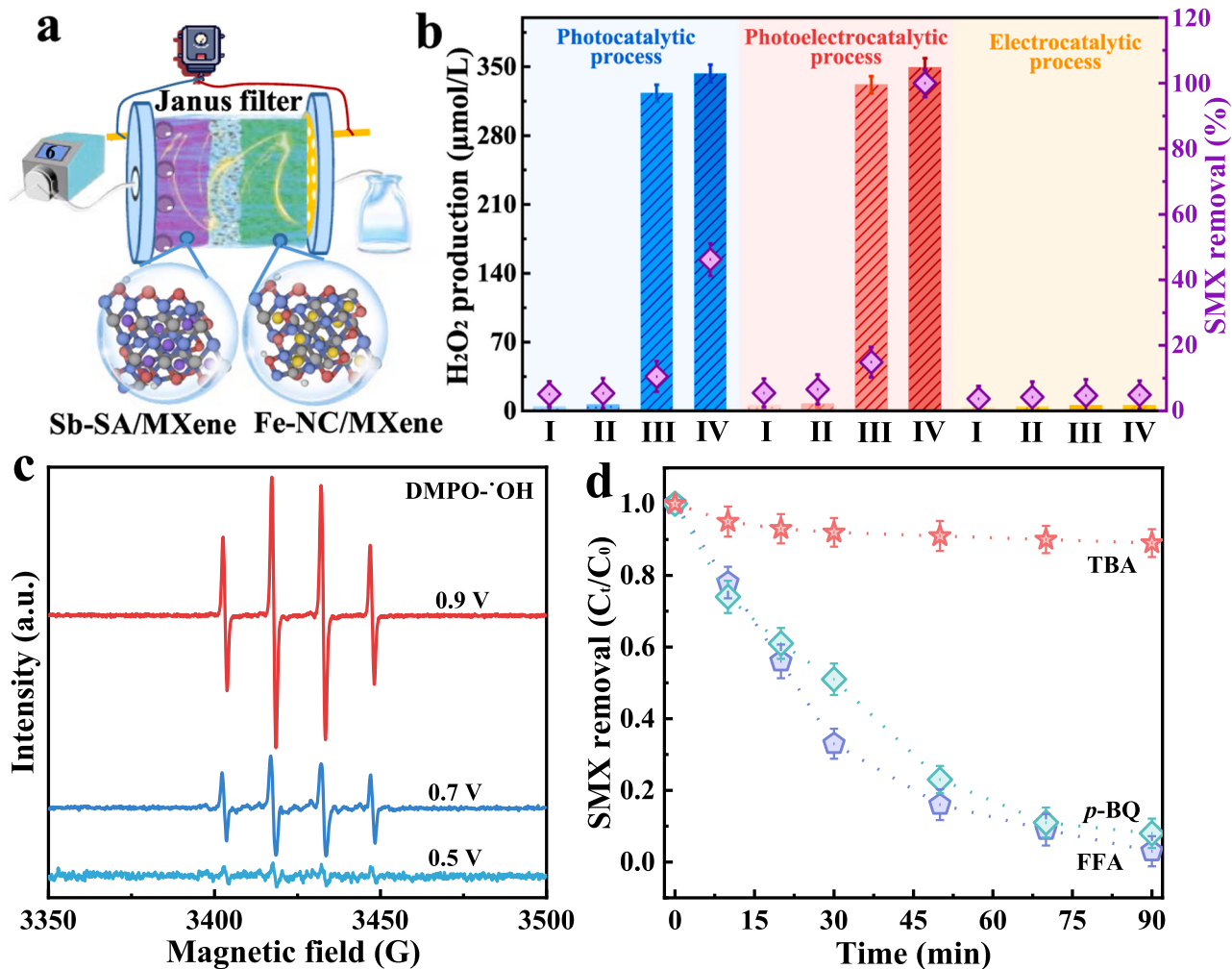


Fig. 2. Photoelectrocatalytic performance of Sb-Fe/MXene filter towards H₂O₂ and •OH production. (a) Schematic illustrating the flow-through system. (b) H₂O₂ production and SMX removal under different filters and photoelectric modes in a phosphate buffer solution. Filters I-IV are for MXene, Fe-NC/MXene, Sb-SA/MXene and Sb-Fe/MXene. (c) EPR signals of DMPO-•OH under different potentials by the Sb-Fe/MXene filter. (d) ROS quenching by applying TBA, FFA and *p*-BQ as quenchers for •OH, ¹O₂ and O₂[•], respectively. Experimental conditions: pH = 6.8, [Na₂SO₄]₀ = 50 mmol/L, cell potential = 0.9 V and flow rate = 6.0 mL/min.

samples, which was ~56 times that from undoped MXene (6.1 μmol/L in 90 min). The surface area of Sb-SA/MXene (6.4 m²/g) was close to that of pristine MXene (6.7 m²/g), indicating that the activity per area was enhanced by introducing the Sb-SA onto MXene. While almost no H₂O₂ (<5 μmol/L within 90 min) was generated in an electrocatalytic process without light illumination on the Sb-SA/MXene, highlighting the indispensable role of the photocatalytic process (Fig. 2b). Furthermore, without added O₂, shown in Fig. S10, no H₂O₂ was produced. Hence, it can be concluded that the H₂O₂ was formed through the 2e⁻ ORR mechanism.

To further investigate the H₂O₂ production process, the reduction and oxidation reactions were isolated on the Sb-SA/MXene by adding either electron donors or electron acceptors to quench the reduction or oxidation process. 2-propanol solution (10 vol%) with saturated O₂ (Fig. S11a) and NaIO₃ solution (20 mmol/L) with saturated N₂ (Fig. S11b) were separately passed through the Sb-SA/MXene surface under visible light. The results confirmed the 2e⁻ ORR mechanism for the H₂O₂ formation. To confirm the involvement of the 4e⁻ WOR, an isotope reaction was carried out using H₂¹⁸O passing through the Sb-SA/MXene surface for 200 min and 500 min under visible light. Fe³⁺/H⁺ was then fed into the reactor to dissociate H₂O₂ and produce O₂. The gaseous products exhibited a strong ¹⁶O₂ peak (91.6%) and a weak ¹⁸O₂ peak (4.7%) after a 200 min reaction (Fig. S12), suggesting that H₂¹⁶O originated from the ¹⁶O₂ reduction at the beginning. After 500 min, the

intensity of the ¹⁸O₂ peak was increased to 16.2%, accompanied by the decrease of the ¹⁶O₂ peak to 77.3%, as shown in Fig. S12. Hence, the O₂ generated from the 4e⁻ WOR was eventually used to produce H₂O₂ in the 2e⁻ ORR process.

3.3. Characterization of Fe-NC/MXene surface

After defining the function of Sb-SA/MXene to produce H₂O₂, we further deposited Fe-NC functionalized Ti₃C₂T_x MXene onto the permeate-side of Ni-foam to strengthen the H₂O₂ decomposition toward organic pollutants degradation. As shown in the HRTEM image (Fig. 1d), these Fe-NC were amorphous and evenly dispersed on the MXene surface with an average particle diameter of 2.0 ± 0.5 nm. The XRD patterns obtained (Fig. S13) for the Fe-NC/MXene surface exhibited crystallinity in the MXene phase, while the absence of characteristic peaks corresponding to Fe-NC indicated its amorphous. To identify the contribution of Ti vacancies to the formation of ultra-small nanoclusters, the local chemical environments of Fe and O species on Fe-NC/MXene were investigated by XPS. As shown in Fig. S14a, the Fe 2p_{3/2} spectrum of Fe-NC/MXene was assigned to the metallic Fe(0) (707.5 eV), Fe (II) (709.3 eV), and Fe(III) (711.8 eV) species. The majority of Fe(0) species are found on the outer surface of MXene, accompanied by a certain proportion of Fe(II) and Fe(III) species resulting from the inevitable oxidation of Fe(0) during synthesis [36]. In addition, The binding

energy of the Fe(0) 2p_{3/2} has a relatively low binding energy with respect to the bulk Fe (Fe(0), 707.7 eV), manifesting that Ti vacancies shift some extra electron density to the nearby Fe sites with an increased electron population [36,37]. Compared with Fe₂O₃ (529.7 eV), the shift of the O 1s peak (Fig. S14b) of Fe-NC/MXene toward lower binding energy could be attributed to the introduction of a Fe–O bond and a Fe–O–Ti unit [38,39]. Based on the ICP-OES analysis, the content of the loaded Fe species was determined to be 8.9 wt%.

3.4. Electrocatalytic •OH generation on Fe-NC/MXene surface

These Fe-NC coated Ti₃C₂T_x MXene were sputtered onto the permeate-side of a Ni-foam to enhance the selectivity of H₂O₂ decomposition. As shown in Fig. S15, the designed Janus Sb-Fe/MXene configuration is critical for boosting the H₂O₂ decomposition compared to a single-side Sb-SA/MXene photocatalytic filter. We first detected the •OH generation using Sb-Fe/MXene photoelectrocatalytic filtration system with only Na₂SO₄ electrolyte as the feed solution assisted by an electric field. Electron paramagnetic resonance (EPR) spectra (Fig. 2c) demonstrated the typical quadrupole peak signal associated with DMPO-•OH adduct with 1:2:2:1 intensities [40], indicating the presence of •OH in the permeate. The EPR intensity of DMPO-•OH decreased without the applied potential (Fig. 2c). When DMPO and TEMP were employed to capture the O₂^{•-} and ¹O₂, respectively, no EPR signals of DMPO-O₂^{•-} and TEMP-¹O₂ adducts were recorded during the photoelectrocatalytic filtration (Fig. S16), suggesting that •OH was the sole active species. Since the side reactions, such as hydrogen and oxygen evolution, were enhanced at high potential with decreased Coulombic efficiency [27,41], a minimum potential of 0.9 V was selected for the following studies.

The efficacy of the proposed Janus photoelectrocatalytic filtration system for removing pollutants in wastewater was quantitatively investigated. An antibiotic, SMX, was chosen as a representative pollutant. As shown in Fig. 2b, the Sb-Fe/MXene filter exhibited a complete SMX removal under flow-through mode within 30 min at 0.9 V. Without the applied potential, the removal efficiency was reduced to 46.2%. Hence, the cycling of ≡ Fe(III)/≡ Fe(II) pairs by the external electric field is important. In stark contrast, negligible SMX removal (<15%) was observed using the feed-side Sb-SA/MXene side only under the same conditions, suggesting pure H₂O₂ produced by photocatalysis can hardly degrade SMX. To further determine the •OH production, chemical quenching experiments using different scavengers on SMX removal were examined. As illustrated in Fig. 2d, the excessive amounts

of *tert*-butanol (TBA, $k(\cdot\text{OH}) = 3.8 \times 10^8 \text{ M}^{-1} \text{ s}^{-1}$) significantly inhibited the SMX removal (87.4%), highlighting that •OH was the prominent ROS in the electrocatalytic system. The presence of *p*-benzoquinone (*p*-BQ) and furfuryl alcohol (FFA) posed a limited effect on the SMX removal (<5%), implying the contribution of O₂^{•-} and ¹O₂ could be excluded. In addition, we compared the SMX removal experiment with a conventional batch reactor. As shown in Fig. S17, the efficiency of removing SMX in a batch reactor was decreased by over 5-fold to 18.4% with a current density of 0.4 mA/cm² due to convection-enhanced mass transport in the flow-through configuration. Furthermore, the Janus Sb-Fe/MXene filter outperformed other individual photocatalytic or electrocatalytic configurations (Table S3). The degradation mechanism with three main reactions involving the •OH is illustrated in Fig. S18, with the TOC removal increasing significantly to 79.1% (Fig. S19).

3.5. Working mechanism of the Sb-Fe/MXene filter

To explore the possible roles of Sb-SA sites in strengthening the photocatalytic H₂O₂ generation, density functional theory (DFT) calculations were initially conducted to unveil their electronic structures. After loading Sb-SA onto the MXene support (Fig. 3a), the electron density was redistributed due to the strong electronic interaction between the Sb atoms and the surrounding O and C atoms, increasing the Bader charge difference from -0.004 e^- to -0.025 e^- , indicating the promoted electron transfer between the Sb-SA and MXene, resulting in higher photocatalytic activities. The O₂ adsorption energy on MXene is only -0.017 eV , much lower than -0.448 eV on the Sb-SA sites, suggesting O₂ is preferably adsorbed on the Sb sites. To understand this preference, the density of states (DOS) was calculated and shown in Fig. 3b for the O₂ bonded on Sb sites. It shows that the O₂ π^* orbital was shifted lower than the Fermi level due to the interaction between the O₂ *p* orbital and the Sb *p* orbital to form a hybridized structure. Electrons are transferred from the Sb to the adsorbed O₂ to form a strong Sb–O bond while activating O₂ [42]. On the other hand, a very small amount of electrons were transferred from MXene to O₂ (Fig. S20), suggesting the interaction between the O₂ and MXene is very weak. Therefore, the Sb-SA sites are expected to have a significant catalytic contribution to ORR.

The optical characteristics and band structure of the Sb-SA/MXene were established with ultraviolet-visible diffuse reflectance spectroscopy (UV-vis DRS, Fig. S21). Introducing Sb-SA slightly reduced the bandgap energy of MXene from 2.5 to 2.3 eV with increased visible light absorption. As confirmed by the Mott-Schottky (Fig. S22) and valence-

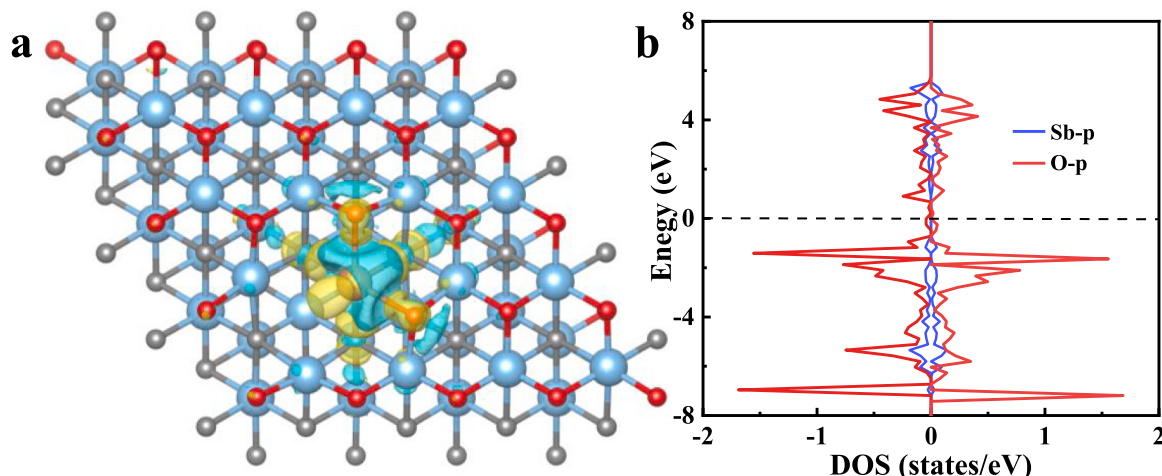
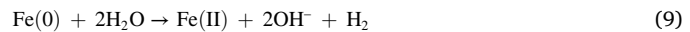
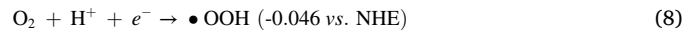


Fig. 3. DFT calculation results. (a) Charge density of Sb-SA sites. (b) DOS of Sb-p and O₂-p orbital, and the interaction within the O₂ chemisorption configuration on Sb-SA sites.

band XPS (Fig. S23) results, the introducing Sb-SA shifts the MXene conduction band slightly from -0.69 to -0.64 eV vs. Ag/AgCl, while the corresponding valence band shifts from 1.83 to 1.70 eV vs. Ag/AgCl. From the above results, the band structure plots of MXene and Sb-SA/MXene were derived and illustrated in Fig. S24. The separation and recombination of photoexcited charge carriers were investigated by steady-state photoluminescence (PL) spectroscopy. After the Sb-SA decoration, the PL intensity from the MXene was significantly reduced (Fig. S25). Hence, the charge recombination was effectively quenched on the Sb-SA/MXene, achieving the best photocatalytic performance with much-enhanced photocurrent density (Fig. S26) and decreased interface resistance from the Nyquist plots (Fig. S27).

Raman spectra (Fig. 4a) were collected under optimal conditions to identify the intermediate. For the pristine MXene surface, after reaction in a 2-propanol solution (10 vol%) under visible light, the C–O vibration band at 892.1 cm^{-1} was observed. However, on the Sb-SA/MXene, the O–O stretching band at 858.7 cm^{-1} was identified from the Sb-OOH moiety in end-on adsorption arrangement [10], supported by the DFT calculations. It was noteworthy that the Sb-OOH can be formed without adding 2-propanol, essential for the exclusive $2e^-$ ORR mechanism [43, 44]. In addition, although O_2^- could also be involved in the formation of

1,4-endoperoxide through the $1e^-$ pathway (Eq. 8), the absence of the DMPO- O_2^- signal in Fig. S28 confirmed that the O_2^- pathway was not feasible under our conditions. Therefore, the $2e^-$ ORR is the only process responsible for the reduction of O_2 , agreed with the Raman results.



The activation mechanism of Fe-NC/MXene toward H_2O_2 decomposition for SMX degradation was further investigated. Initially, H_2O_2 generated on the Sb-SA/MXene photocatalytic surface diffused to Fe-NC/MXene electrocatalytic surface. Hereafter, the cycling of $\equiv \text{Fe}(0) \leftrightarrow \equiv \text{Fe}(\text{II}) \leftrightarrow \equiv \text{Fe}(\text{III})$ occurred on the Fe-NC/MXene surface and facilitated the H_2O_2 activation to produce a strong $\bullet\text{OH}$ signal. Notably, the disappearance of $\text{Fe}(0)$ and the ratio of $\text{Fe}(\text{II})/\text{Fe}_{\text{total}}$ in Fe-NC/MXene surface increased from 27.5% to 43.1% after the electrocatalytic reaction, indicating the surface $\text{Fe}(\text{II})$ generation derived from Fe-NC oxidation (Fig. 4b). It is widely accepted that $\text{Fe}(0)$ could react with dissolved oxygen and/or water through Eqs. 9–10, resulting in the

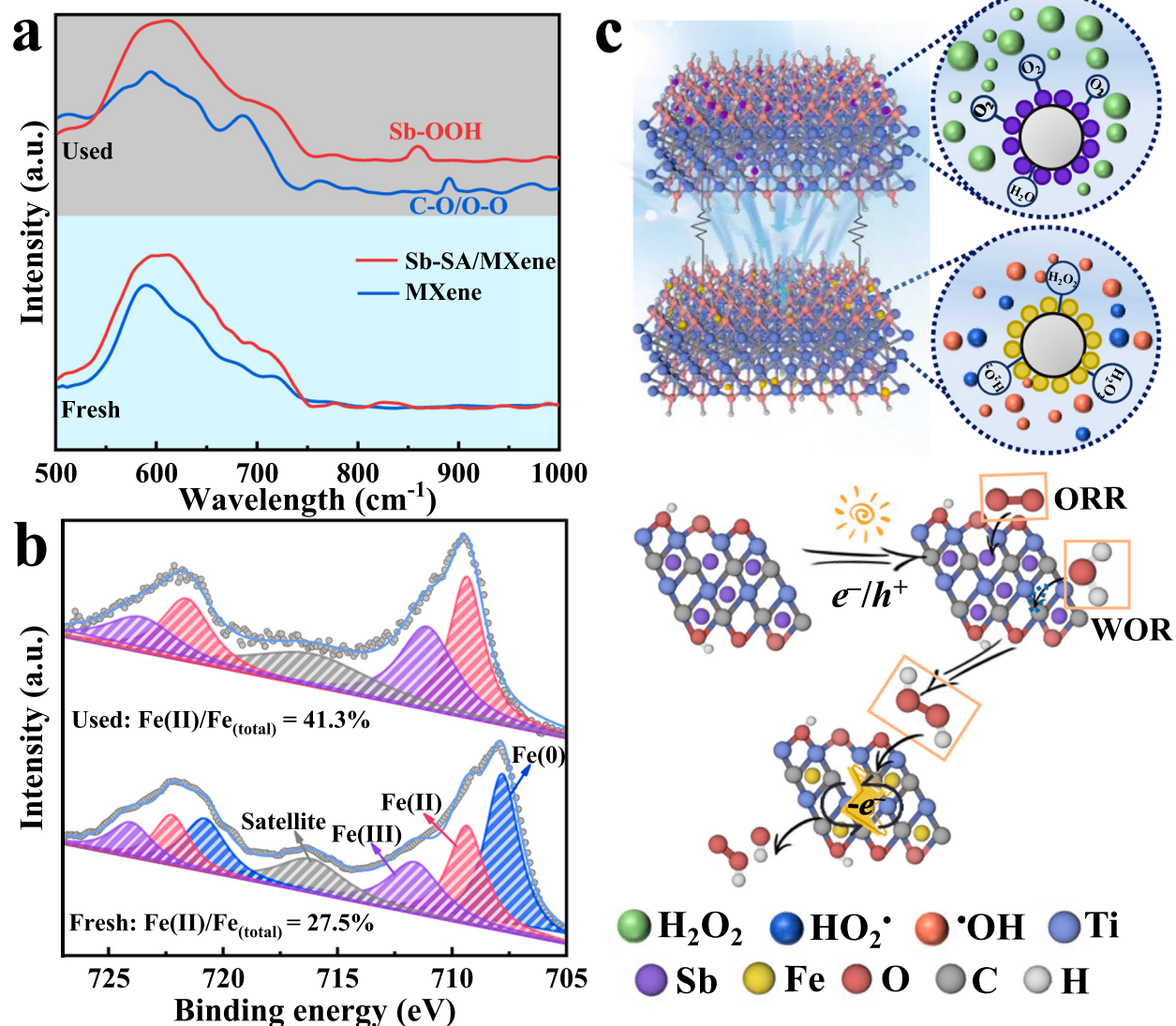


Fig. 4. Photoelectrochemical properties of Sb-Fe/MXene filter. (a) Raman spectra were recorded during the ORR process. MXene filter in 2-propanol solution with saturated O_2 , Sb-SA/MXene in pure water. (b) XPS spectra for Fe 2p of Fe-NC/MXene surface before and after the electrocatalytic reaction. (c) Schematic of the Sb-SA/MXene photocatalytic surface with H_2O_2 generation and the Fe-NC/MXene electrocatalytic surface with $\bullet\text{OH}$ production concurrently.

formation of active \equiv Fe(II) sites [45]. Similar to the traditional Fenton systems, \equiv Fe(II) had a more negative reduction potential resulting in a stronger catalytic activity for H_2O_2 decomposition, while the conversion from \equiv Fe(III) to \equiv Fe(II) was a rate-limiting step of the whole cycle [46, 47]. The applied electric field can be used to recover Fe(II) in the current system, which would donate an electron to \equiv Fe(III), giving rise to \equiv Fe(II) sites. The increased XPS peak intensity of \equiv Fe(II) with respect to \equiv Fe(III) at a total cell potential of 0.9 V was observed in Fig. 4b, suggesting the electrochemical potential drives the reduction of \equiv Fe(III) to the reactive \equiv Fe(II). In addition, the presence of Ti vacancies lowers the binding energy of Fe 2p than that of bulky Fe_2O_3 (Fig. 4b) at 0.9 V [48], suggesting the formation of high electron population around the Fe-NC sites improves the H_2O_2 conversion to $\cdot\text{OH}$ effectively.

Based on the above characterization and analysis, the reaction mechanisms for photocatalytic H_2O_2 production and electrocatalytic HO^\bullet generation with a Janus Sb-Fe/MXene filter is proposed as follows (Fig. 4c): On the feed-side, effective separation of photoexcited charge carriers happens on the Sb-SA/MXene surface. Under visible light, excited electrons are photocatalytically generated to reduce O_2 through $2e^-$ ORR. Meanwhile, the H_2O is oxidized by the holes localized at the Ti vacancies near Sb single-atoms to maintain the $2e^-$ ORR by producing O_2 . On the permeate-side, the efficient activation of H_2O_2 into $\cdot\text{OH}$ by the Fe-NC/MXene surface was attributed to the unique promotion effect of the electric field and flow-through design. The introduction of an electric field was favorable to boosting the rapid and stable conversion of \equiv Fe(III) to \equiv Fe(II), and then the active \equiv Fe(II) reacted with H_2O_2 to generate $\cdot\text{OH}$ for wastewater purification. The flow-through configuration also promoted the reaction kinetics, further contributing to efficient organic decontamination.

3.6. Practical application of Sb-Fe/MXene filter

A rapid rise in Sb(III) pollution in the environment could be a major concern for human health [49,50]. Unlike other pollutants, removing Sb(III) via adsorption can form a highly reactive photocatalyst for waste utilization under certain conditions, which is believed to offer a “win-win” strategy in terms of environmental benefit and resource recovery. For proof-of-concept, we recovered Sb(III) from lake water (spiked with Sb(III) and SMX) as a photocatalyst to create a photoelectrocatalytic filtration system. As shown in Fig. 5a, filter composed of pure MXene at the feed-side and Fe-NC/MXene at the permeate-side offered a high removal efficiency for Sb(III) (97.1%) and SMX (94.7%). Significantly, this process provides a green strategy towards sustainable environmental remediation in a “treating waste by waste” principle.

To evaluate the feasibility in practical application, the long-term activity of the Sb-Fe/MXene filter was investigated by monitoring the consecutive H_2O_2 generation and SMX degradation. The reproducibility of Sb-Fe/MXene filter was more than 93% for H_2O_2 production and SMX degradation after five photoelectrocatalytic runs (Fig. 5b). While the leached Sb (0.6 wt%; $<6 \mu\text{g/L}$) and Fe (9.4 wt%; $<300 \mu\text{g/L}$) from the Sb-Fe/MXene photoelectrocatalytic system were way below the limits specified by the US Environmental Protection Agency and World Health Organization (Fig. S29) [50,51]. Meanwhile, the Sb-Fe/MXene photoelectrocatalytic system exhibited excellent stability during the SMX degradation with minimal performance decay (<12%) after 24 h continuous operation. Notably, both surface morphologies (Fig. S30) and crystalline phase (Fig. S31) analyses of the Sb-Fe/MXene filter suggested a negligible change on the physicochemical characteristics before and after the reaction, thus, demonstrating an excellent chemical and structural robustness of the filter. In addition, energy consumption was another important aspect to evaluate the economic efficiency of the photoelectrocatalytic system. The proposed Sb-Fe/MXene system required low energy consumption of 0.04 kWh/g SMX at 0.9 V with the corresponding current of 2.4 mA at pH neutral (Text S4), which is better than most of the electrochemical systems (Table S3).

4. Conclusion

In summary, we have developed a Janus Sb-Fe/MXene photoelectrocatalytic filter to leverage sequential reduction reactions in the feed- and permeate-side for efficient H_2O_2 and $\cdot\text{OH}$ yield via a flow-through mode, respectively, offering a sustainable and reagent-free strategy for water decontamination in a manner of “treating waste by waste”. Both experimental and theoretical studies show that the Sb-SA with the d^{10} electronic configuration is appropriate for forming high electron and hole densities, leading to a highly efficient non-sacrificial H_2O_2 synthesis through the photocatalytic $2e^-$ ORR pathway. Simultaneously, the accumulated holes neighboring the Ti vacancies accelerated *in situ* generating O_2 via the $4e^-$ WOR. These O_2 species were further reduced by the $2e^-$ ORR to boost overall H_2O_2 production. On the electrocatalytic-active side, the electrochemical potential constantly reduces the \equiv Fe(III) to \equiv Fe(II) under pH-neutral conditions. Such exposed “fresh” active sites are essential for dissociating H_2O_2 to produce reactive $\cdot\text{OH}$, while effectively limiting the accumulation of iron sludge. As a result, the degradation of organic pollutants is effectively enhanced even in actual wastewater. We further demonstrate that the high degradation efficiency of organic pollutants was mainly due to the convection-enhanced mass transportation driven by the flow-through

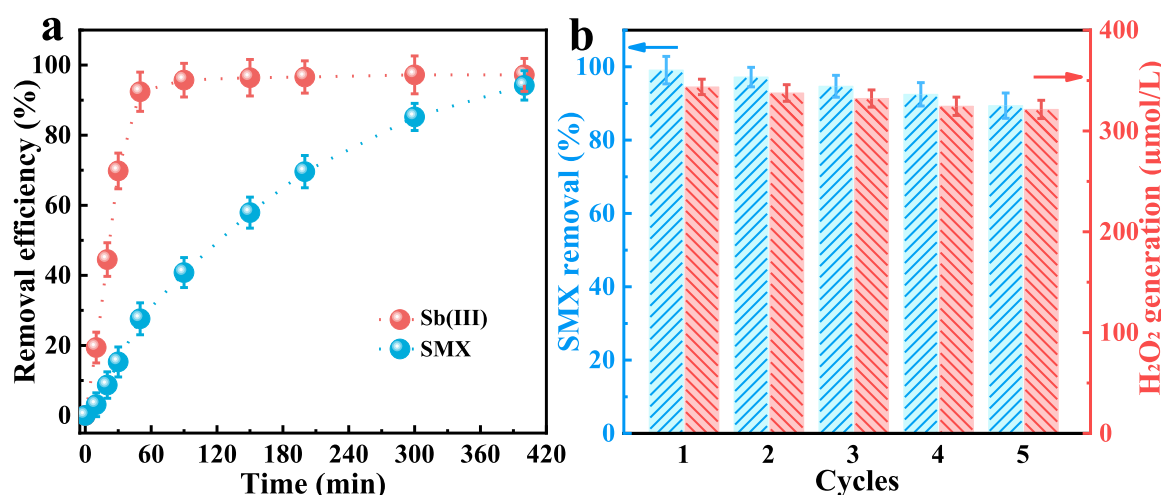


Fig. 5. Practical application of Sb-Fe/MXene Janus filter. (a) The removal efficiency of Sb(III) and SMX by pure MXene at the feed-side and Fe-NC/MXene at the permeate-side simultaneously. (b) Repeatability of Sb-Fe/MXene filter for H_2O_2 production and SMX degradation.

configuration. Moreover, the designed Janus photoelectrocatalytic filter represents a novel system significantly different from the simple assembly of half-cell reactions with a filter substrate. It presents a smart design strategy for a high-performance and multifunctional photoelectrocatalytic filter.

CRediT authorship contribution statement

Limin Jin: Investigation, Data curation, Methodology, Writing – original draft. **Meng Sun:** Validation, Formal analysis, Supervision. **Jianping Yang:** Conceptualization, Formal analysis. **Yingping Huang:** Formal analysis. **Yanbiao Liu:** Funding acquisition, Conceptualization, Writing – review & editing, Supervision.

Declaration of Competing Interest

The authors declare that they have no known competing financial interests or personal relationships that could have appeared to influence the work reported in this paper.

Data Availability

Data will be made available on request.

Acknowledgments

Project supported by the National Natural Science Foundation of China (No. 52170068, 21972073 and 22136003), the Natural Science Foundation of Shanghai (23ZR1401300) and the Fundamental Research Funds for the Central Universities (2232023A-08).

Appendix A. Supporting information

Supplementary data associated with this article can be found in the online version at [doi:10.1016/j.apcatb.2023.123150](https://doi.org/10.1016/j.apcatb.2023.123150).

References

- [1] B.C. Hedges, E.L. Cates, J.H. Kim, Challenges and prospects of advanced oxidation water treatment processes using catalytic nanomaterials, *Nat. Nanotechnol.* 13 (2018) 642–650.
- [2] Y.X. Ye, J.H. Pan, F.Y. Xie, L. Gong, S.M. Huang, Z.F. Ke, F. Zhu, J.Q. Xu, G. F. Ouyang, Highly efficient photosynthesis of hydrogen peroxide in ambient conditions, *Proc. Natl. Acad. Sci. USA* 118 (2021) 2103964118.
- [3] J. Xu, X. Zheng, Z. Feng, Z. Lu, Z. Zhang, W. Huang, Y. Li, D. Vuckovic, Y. Li, S. Dai, G. Chen, K. Wang, H. Wang, J.K. Chen, W. Mitch, Y. Cui, Organic wastewater treatment by a single-atom catalyst and electrolytically produced H_2O_2 , *Nat. Sustain.* 4 (2021) 233–241.
- [4] Z. Zhang, T. Tsuchimochi, T. Ina, Y. Kumabe, S. Muto, K. Ohara, H. Yamada, S. L. Ten no, T. Tachikawa, Binary dopant segregation enables hematite-based heterostructures for highly efficient solar H_2O_2 synthesis, *Nat. Commun.* 13 (2022) 1499.
- [5] S. Yang, A. Verdaguera Casadevall, L. Arnarson, L. Silvioli, V. Čolić, R. Frydendal, J. Rossmeisl, I. Chorkendorff, I.E.L. Stephens, Toward the decentralized electrochemical production of H_2O_2 : A focus on the catalysis, *ACS Catal.* 8 (2018) 4064–4081.
- [6] Y.B. Liu, J.H. Li, B.X. Zhou, J. Bai, Q. Zheng, J.L. Zhang, W.M. Cai, Comparison of photoelectrochemical properties of TiO_2 -nanotube-array photoanode prepared by anodization in different electrolyte, *Environ. Chem. Lett.* 7 (2009) 363–368.
- [7] D. Iglesias, A. Giuliani, M. Melchionna, S. Marchesan, A. Criado, L. Nasi, M. Bevilacqua, C. Tavagnacco, F. Vizza, M. Prato, P. Fornasiero, N-doped graphitized carbon nanohorns as a forefront electrocatalyst in highly selective O_2 reduction to H_2O_2 , *Chem* 4 (2018) 106–123.
- [8] Y. Ding, S. Maitra, S. Halder, C. Wang, R. Zheng, T. Barakat, S. Roy, L.H. Chen, B. L. Su, Emerging semiconductors and metal-organic-compounds-related photocatalysts for sustainable hydrogen peroxide production, *Matter* 5 (2022) 2119–2167.
- [9] C. Chu, Q. Zhu, Z. Pan, S. Gupta, D. Huang, Y. Du, S. Weon, Y. Wu, C. Muhich, E. Stavitski, K. Domen, J.H. Kim, Spatially separating redox centers on 2D carbon nitride with cobalt single atom for photocatalytic H_2O_2 production, *Proc. Natl. Acad. Sci. USA* 117 (2020) 6376–6382.
- [10] Z.Y. Teng, Q.T. Zhang, H.B. Yang, K. Kato, W.J. Yang, Y.R. Lu, S.X. Liu, C.Y. Wang, A. Yamakata, C. Su, B. Liu, T. Ohno, Atomically dispersed antimony on carbon nitride for the artificial photosynthesis of hydrogen peroxide, *Nat. Catal.* 4 (2021) 374–384.
- [11] L.B. Xie, P.F. Wang, Y. Li, D.P. Zhang, D.H. Shang, W.W. Zheng, Y.G. Xia, S. H. Zhan, W.P. Hu, Pauling-type adsorption of O_2 induced electrocatalytic singlet oxygen production on N-CuO for organic pollutants degradation, *Nat. Commun.* 13 (2022) 5560.
- [12] K.Y. Chen, Y.X. Huang, R.C. Jin, B.C. Huang, Single atom catalysts for use in the selective production of hydrogen peroxide via two-electron oxygen reduction reaction: Mechanism, activity, and structure optimization, *Appl. Catal. B-Environ.* 337 (2023), 122987.
- [13] M.M. Montemore, M.A. van Spronsen, R.J. Madix, C.M. Friend, O_2 activation by metal surfaces: Implications for bonding and reactivity on heterogeneous catalysts, *Chem. Rev.* 118 (2018) 2816–2862.
- [14] E. Jung, H. Shin, B.H. Lee, V. Efremov, S. Lee, H.S. Lee, J. Kim, W. Hooch Antink, S. Park, K.S. Lee, S.P. Cho, J.S. Yoo, Y.E. Sung, T. Hyeon, Atomic-level tuning of Co-N-C catalyst for high-performance electrochemical H_2O_2 production, *Nat. Mater.* 19 (2020) 436–442.
- [15] Z.Y. Teng, W. Cai, W. Sim, Q. Zhang, C. Wang, C. Su, T. Ohno, Photoexcited single metal atom catalysts for heterogeneous photocatalytic H_2O_2 production: Pragmatic guidelines for predicting charge separation, *Appl. Catal. B-Environ.* 282 (2021), 119589.
- [16] S. Meng, P. Zhou, Y. Sun, P. Zhang, C. Zhou, Z. Xiong, H. Zhang, J. Liang, B. Lai, Reducing agents enhanced Fenton-like oxidation (Fe(III)/Peroxydisulfate): Substrate specific reactivity of reactive oxygen species, *Water Res.* 218 (2022), 118412.
- [17] A.L.T. Pham, C. Lee, F.M. Doyle, D.L. Sedlak, A silica-supported iron oxide catalyst capable of activating hydrogen peroxide at neutral pH values, *Environ. Sci. Technol.* 43 (2009) 8930–8935.
- [18] F. Chen, X.L. Wu, C.Y. Shi, H.J. Lin, J.R. Chen, Y.P. Shi, S.B. Wang, X.G. Duan, Molecular engineering toward pyrrolic N-rich M-N₄ (M = Cr, Mn, Fe, Co, Cu) single-atom sites for enhanced heterogeneous Fenton-like reaction, *Adv. Funct. Mater.* 31 (2021) 2007877.
- [19] L.C. Wang, L.C. Chang, W.Q. Chen, Y.H. Chien, P.Y. Chang, C.W. Pao, Y.F. Liu, H. S. Sheu, W.P. Su, C.H. Yeh, C.S. Yeh, Atomically dispersed golds on degradable zero-valent copper nanocubes augment oxygen driven Fenton-like reaction for effective orthotopic tumor therapy, *Nat. Commun.* 13 (2022) 7772.
- [20] D.L. Guo, Y. Wang, P. Lu, J. Liu, Y.B. Liu, Flow-through electro-Fenton using nanoconfined Fe-Mn bimetallic oxides: Ionization potential-dependent micropollutants degradation mechanism, *Appl. Catal. B-Environ.* 328 (2023), 122538.
- [21] Y. Yin, W. Li, C. Xu, L. Shi, L.C. Zhang, Z. Ao, M. Liu, M. Lu, X. Duan, S. Wang, S. Liu, H. Sun, Ultrafine copper nanoclusters and single sites for Fenton-like reactions with high atom utilities, *Environ. Sci. Nano* 7 (2020) 2595–2606.
- [22] D.N. Nguyen, G.S. Gund, M.G. Jung, S.H. Roh, J. Park, J.K. Kim, H.S. Park, Core-shell structured MXene@Carbon nanodots as bifunctional catalysts for solar-assisted water splitting, *ACS Nano* 14 (2020) 17615–17625.
- [23] A. Vahid Mohammadi, J. Rosen, Y. Gogotsi, The world of two-dimensional carbides and nitrides (MXenes), *Science* 372 (2021) 1581.
- [24] Y.B. Liu, G.D. Gao, C.D. Vecitis, Prospects of an electroactive carbon nanotube membrane toward environmental applications, *Acc. Chem. Res.* 53 (2020) 2892–2902.
- [25] L.M. Jin, S.J. You, Y. Yao, H. Chen, Y. Wang, Y.B. Liu, An electroactive single-atom copper anchored MXene nanohybrid filter for ultrafast water decontamination, *J. Mater. Chem. A* 9 (2021) 25964–25973.
- [26] M. Faraji, M. Yousefi, S. Yousefzadeh, M. Zirak, N. Naseri, T.H. Jeon, W. Choi, A. Z. Moshfegh, Two-dimensional materials in semiconductor photoelectrocatalytic systems for water splitting, *Energy Environ. Sci.* 12 (2019) 59–95.
- [27] Y.M. Zhao, M. Sun, X.X. Wang, C. Wang, D.W. Lu, W. Ma, S.A. Kube, J. Ma, M. Elimelech, Janus electrocatalytic flow-through membrane enables highly selective singlet oxygen production, *Nat. Commun.* 11 (2020) 6228.
- [28] M. Alhabeb, K. Maleski, B. Anasori, P. Lelyukh, L. Clark, S. Sin, Y. Gogotsi, Guidelines for synthesis and processing of two-dimensional titanium carbide ($Ti_3C_2T_x$ MXene), *Chem. Mater.* 29 (2017) 7633–7644.
- [29] W.J. Jiang, Y.B. Liu, F.Q. Liu, F. Li, C.S. Shen, B. Yang, M.H. Huang, J.S. Liu, Z. W. Wang, W. Sand, Ultra-fast detoxification of Sb(III) using a flow-through TiO_2 -nanotubes-array-mesh based photoelectrochemical system, *Chem. Eng. J.* 387 (2020), 124155.
- [30] L. Li, J.H. Li, F. Fang, Y. Zhang, T. Zhou, C. Zhou, J. Bai, B. Zhou, Efficient H_2O_2 production from urine treatment based on a self-biased WO_3/TiO_2 -Si PVC photoanode and a $WO_3/CMK-3$ cathode, *Appl. Catal. B-Environ.* 333 (2023), 122776.
- [31] A.Q. Wang, J. Li, T. Zhang, Heterogeneous single-atom catalysis, *Nat. Rev. Chem.* 2 (2018) 65–81.
- [32] S.K. Kaiser, Z. Chen, D. Faust Akl, S. Mitchell, J. Pérez Ramírez, Single-atom catalysts across the periodic table, *Chem. Rev.* 120 (2020) 11703–11809.
- [33] C. Tsounis, B. Subhash, P.V. Kumar, N.M. Bedford, Y. Zhao, J. Shenoy, Z. Ma, D. Zhang, C.Y. Toe, S. Cheong, R.D. Tilley, X. Lu, L. Dai, Z. Han, R. Amal, Pt single atom electrocatalysts at graphene edges for efficient alkaline hydrogen evolution, *Adv. Funct. Mater.* 32 (2022) 2203067.
- [34] L.L. Wang, C.W. Zhu, M.Q. Xu, C.L. Zhao, J. Gu, L. Cao, X.H. Zhang, Z.H. Sun, S. Q. Wei, W. Zhou, W.X. Li, J.L. Lu, Boosting activity and stability of metal single-atom catalysts via regulation of coordination number and local composition, *J. Am. Chem. Soc.* 143 (2021) 18854–18858.
- [35] W.S. Ma, J.W. Wang, H. Gao, J.Z. Niu, F.K. Luo, Z.Q. Peng, Z.H. Zhang, A mesoporous antimony-based nanocomposite for advanced sodium ion batteries, *Energy Stor. Mater.* 13 (2018) 247–256.

[36] H.Y. Fu, M.R. Li, Q.Y. Xu, G.L. Chen, Y.J. Zou, W.X. Zhang, S.Z. Li, L. Ling, Nitrogen doped carbon-distributed and nitrogen-stabilized ultrafine FeM (M = Pd, Pt, Au) nanoclusters for doxorubicin detoxification, *Appl. Catal. B-Environ.* 316 (2022), 121646.

[37] S.R. Yang, C.S. He, Z.H. Xie, L.L. Li, Z.K. Xiong, H. Zhang, P. Zhou, F. Jiang, Y. Mu, B. Lai, Efficient activation of PAA by FeS for fast removal of pharmaceuticals: The dual role of sulfur species in regulating the reactive oxidized species, *Water Res.* 217 (2022), 118402.

[38] S. Huang, T. Ouyang, B.F. Zheng, M. Dan, Z.Q. Liu, Enhanced photoelectrocatalytic activities for CH₃OH-to-HCHO conversion on Fe₂O₃/MoO₃; Fe-O-Mo covalency dominates the intrinsic activity, *Angew. Chem. Int. Ed.* 60 (2021) 9546–9552.

[39] S. Parvin, D.K. Chaudhary, A. Ghosh, S. Bhattacharyya, Attuning the electronic properties of two-dimensional Co-Fe-O for accelerating water electrolysis and photolysis, *ACS Appl. Mater. Interfaces* 11 (2019) 30682–30693.

[40] L.M. Jin, S.J. You, X.G. Duan, Y. Yao, J.M. Yang, Y.B. Liu, Peroxymonosulfate activation by Fe₃O₄-MnO₂/CNT nanohybrid electroactive filter towards ultrafast micropollutants decontamination: Performance and mechanism, *J. Hazard. Mater.* 423 (2022), 127111.

[41] Y. Yang, G. Banerjee, G.W. Brudvig, J.H. Kim, J.J. Pignatello, Oxidation of organic compounds in water by unactivated peroxyxmonosulfate, *Environ. Sci. Technol.* 52 (2018) 5911–5919.

[42] T. Wang, X. Cao, H. Qin, L. Shang, S. Zheng, F. Fang, L. Jiao, P-block atomically dispersed antimony catalyst for highly efficient oxygen reduction reaction, *Angew. Chem. Int. Ed.* 60 (2021) 21237–21241.

[43] C.H. Chu, D. Huang, Q. Zhu, E. Stavitski, J.A. Spies, Z. Pan, J. Mao, H.L. Xin, C. A. Schmuttenmaer, S. Hu, J.H. Kim, Electronic tuning of metal nanoparticles for highly efficient photocatalytic hydrogen peroxide production, *ACS Catal.* 9 (2019) 626–631.

[44] A. Kanthe, A. Ilott, M. Krause, S. Zheng, J. Li, W. Bu, M.K. Bera, B. Lin, C. Maldarelli, R.S. Tu, No ordinary proteins: Adsorption and molecular orientation of monoclonal antibodies, *Sci. Adv.* 7 (2021) 2873.

[45] X. Zhang, H.W. Sun, Y.B. Shi, C.C. Ling, M.Q. Li, C. Liang, F.L. Jia, X. Liu, L. Zhang, Z.H. Ai, Oxalated zero valent iron enables highly efficient heterogeneous Fenton reaction by self-adapting pH and accelerating proton cycle, *Water Res.* 235 (2023), 119828.

[46] L.M. Jin, S.J. You, N.Q. Ren, B. Ding, Y.B. Liu, Mo vacancy-mediated activation of peroxyxmonosulfate for ultrafast micropollutant removal using an electrified MXene filter functionalized with Fe single atoms, *Environ. Sci. Technol.* 56 (2022) 11750–11759.

[47] A. Serra Clusellas, L. De Angelis, C.H. Lin, P. Vo, M. Bayati, L. Sumner, Z. Lei, N. B. Amaral, L.M. Bertini, J. Mazza, L.R. Pizzio, J.D. Stripeikis, J.A. Rengifo Herrera, M.M. Fidalgo de Cortalezzi, Abatement of 2,4-D by H₂O₂ solar photolysis and solar photo-Fenton-like process with minute Fe(III) concentrations, *Water Res.* 144 (2018) 572–580.

[48] L.N. Su, P.F. Wang, X.L. Ma, J.H. Wang, S.H. Zhan, Regulating local electron density of iron single sites by introducing nitrogen vacancies for efficient photo-Fenton process, *Angew. Chem. Int. Ed.* 60 (2021) 21261–21266.

[49] Y.B. Liu, P. Wu, F.Q. Liu, F. Li, X.Q. An, J.S. Liu, Z.W. Wang, C.S. Shen, W. Sand, Electroactive modified carbon nanotube filter for simultaneous detoxification and sequestration of Sb(III), *Environ. Sci. Technol.* 53 (2019) 1527–1535.

[50] Y.F. Ren, Y.B. Liu, F.Q. Liu, F. Li, C.S. Shen, Z.C. Wu, Extremely efficient electro-Fenton-like Sb(III) detoxification using nanoscale Ti-Ce binary oxide: An effective design to boost catalytic activity via non-radical pathway, *Chin. Chem. Lett.* 32 (2021) 2519–2523.

[51] D.L. Guo, Y.B. Liu, H.D. Ji, C.C. Wang, B. Chen, C.S. Shen, F. Li, Y.X. Wang, P. Lu, W. Liu, Silicate-enhanced heterogeneous flow-through electro-Fenton system using iron oxides under nanoconfinement, *Environ. Sci. Technol.* 55 (2021) 4045–4053.